Decomposition behavior and reaction mechanism of $Ce_{0.67}Tb_{0.33}MgAl_{11}O_{19}$ during Na_2CO_3 assisted roasting
Toward efficient recycling of Ce and Tb from waste phosphor

Hua, Zhongsheng; Geng, Ao; Zhao, Zhuo; Liu, Huan; Yao, Yonglin; Yang, Yongxiang

Important note
To cite this publication, please use the final published version (if applicable).
Please check the document version above.

Research article

Decomposition behavior and reaction mechanism of $Ce_{0.67}Tb_{0.33}MgAl_{11}O_{19}$ during Na_2CO_3 assisted roasting: Toward efficient recycling of Ce and Tb from waste phosphor

Zhongsheng Hua[a,b], Ao Geng[a], Zetao Tang[a], Zhuo Zhao[a,b,*], Huan Liu[a], Yonglin Yao[a], Yongxiang Yang[a,c]

[a] School of Metallurgical Engineering, Anhui University of Technology, Maxiang Road, Ma'anshan, 243032, China
[b] Key Laboratory of Metallurgical Emission Reduction & Resources Recycling (Anhui University of Technology), Ministry of Education, 59 Hudong Road, Ma'anshan, 243002, China
[c] Department of Materials Science and Engineering, Delft University of Technology, Mekelweg 2, 2628 CD, Delft, the Netherlands

A B S T R A C T

Waste aluminate phosphor is a valuable secondary resource of rare earth elements (REEs). However, Ce and Tb in aluminate green phosphor can hardly be extracted by direct leaching in an inorganic acid. Therefore, Na_2CO_3 assisted roasting is adopted to decompose the stable spinel structure of $Ce_{0.67}Tb_{0.33}MgAl_{11}O_{19}$ in the present work and to achieve the transformation of REEs to simple oxides. Based on the thermodynamic calculations, systematic experiments of thermal decomposition have been conducted. The thermal decomposition behavior, phase evolution, valence state change, variations in micro and macro morphology of the green phosphor during Na_2CO_3 assisted roasting were examined by using TG-DSC/MS, XRD, XPS, SEM/EDS analyses. The results indicated that the green phosphor began to react with solid Na_2CO_3 at 800 °C, and the reaction was dramatically accelerated with temperature rising above 851 °C. At about 1000 °C, $Ce_{0.67}Tb_{0.33}MgAl_{11}O_{19}$ could completely decomposed into CeO_2, Tb_2O_3 and MgO by roasting in an equivalent mass of Na_2CO_3 for 2 h, while α-Al_2O_3 was hardly attacked in roasting. The decomposition mechanism of $Ce_{0.67}Tb_{0.33}MgAl_{11}O_{19}$ in molten Na_2CO_3 could be depicted by the unreacted shrinking core model, and the reaction rate constant was estimated at approximately nanometers per second. The synergistic effect of cation-oxoanion ensures the successful extraction of CeO_2 and Tb_2O_3 from the green phosphor via Na_2CO_3 assisted roasting method. The converted CeO_2 and Tb_2O_3 can be extracted by using chlorination roasting and separated from non-REE residues. According to these investigations, a new efficient process technology is proposed for sustainable recycling of waste phosphor.

1. Introduction

Rare earth elements (REEs) have received increasing attention in the transition to a green, low-carbon economy due to their specific physical and chemical properties (Binnemans et al., 2013; De Oliveira et al., 2017; Moldoveanu and Papangelakis, 2012; Vahidi and Zhao, 2017). Meanwhile, with their continually expanding applications in traditional industries, high-tech products, and defense and security technology, REEs are considered as the essential strategic resources (Alam et al., 2012; Favot and Massarutto, 2019). In recent years, the global demand for REEs is growing rapidly. The large and increasing demand causes a supply shortage in REEs market in recent years. Recycling REEs from waste products could mitigate the resource scarcity in the long term. Because it contains a large amount of REEs, the

recycling of waste tricolor phosphor is of great importance for resource conservation, as well as environment protection.

Tricolor phosphor could generally be classified into four categories, including borate, silicate, phosphate and aluminate systems. Currently, the spinel aluminate phosphors have become the most widely used fluorescent materials because of their fairly high stability and luminous efficiency, and are mass-produced all over the world (Wu et al., 2014). Therefore, much attention has been paid to the aluminate system for REE recycling from waste phosphor due to the large amount. Generally, both of the physical and chemical methods could be used to process waste phosphor. Red, green and blue powders can be separately extracted from waste phosphor and thus be reused at a relatively low cost using physical method (Takahashi et al., 2011; Mei et al., 2009; Leblebici et al., 2016). Reuse of the separated phosphor in new lamps

---

Table 1
Chemical composition of the original green phosphor powder (wt.%).

Al_2O_3	CeO_2	Tb_4O_7	MgO	ZnO	Fe_2O_3	CaO	Na_2O	Y_2O_3	Cs_2O	TiO_2	SrO	K_2O	I
87.76	6.55	3.76	1.95	0.05	0.0114	0.0097	0.0069	0.0062	0.0043	0.0021	0.0016	0.0011	0.0019

seems to be the best option for waste phosphor. However, this is applicable only for the production waste or rejects. For the end-of-life (EOL) or spent phosphor, besides the disadvantages of the low recovery efficiency, serious secondary pollution and complicated processing steps (Wu et al., 2014; Liang et al., 2016), the physical regeneration method cannot be recommended because it is difficult to obtain very pure tricolor phosphor (Binnemans et al., 2013). Therefore, chemical method is always employed to extract single and pure REE from EOL waste phosphors.

The full dissolution of targeted REEs into leach solution is critical for a successful metallurgical recovery of REEs from waste phosphor, and it depends very much on the crystal structures of the phosphors. The red phosphor $Y_2O_3:Eu^{3+}$ can be readily dissolved in an inorganic acid solution (Yang et al., 2012; Rabah, 2008), while the aluminate green phosphor $CeMgAl_{11}O_{19}:Tb^{3+}$ and the blue phosphor $BaMgAl_{10}O_{17}:Eu^{2+}$ can hardly be chemically attacked by inorganic acid under moderate conditions (Wu et al., 2014; Tan et al., 2015), and they are just partly dissolved even during hot acid leaching. It is also found that leaching with acids gives higher yttrium recovery than leaching with ammonia (De Michelis et al., 2011). The selection of the specific acid relies mainly on the subsequent processing of the leaching liquor. Sulfuric acid is preferred for selective precipitation, whereas hydrochloric or nitric acid is more applicable to solvent extraction. Mechanochemical treatment is a promising pretreatment method for acid leaching because it is effective in creating disorder in the crystal structure, and thus shows technical advantages in facilitating reaction rate and lowering reaction temperature. Mechanochemical leaching could significantly improve the leaching rate of Y and Eu in the waste phosphor at ambient temperature. However, it is not effective for the leaching of Ce, Tb in the green phosphor (Zhang et al., 2000). Both $CeMgAl_{11}O_{19}:Tb^{3+}$ and $BaMgAl_{10}O_{17}:Eu^{2+}$ are in spinel structures (Zhang et al., 2016). The chemical structures are extremely stable and resistant to acid attack. Practically, alkali fusion can destruct the compounds that are difficult to dissolve, and thus is often used to extract valuable elements from insoluble materials. NaOH is a strong alkali reagent which can destroy the spinel structures under high temperature and covert REEs in the aluminate phosphor into oxides (Zhang et al., 2015; Liu et al., 2015). It was found that the mass ratio of NaOH/waste phosphor, roasting temperature and time were critical for alkali fusion, and the total leaching efficiency of the REEs was enhanced, close to 100% under the condition of mass ratio 6:1, roasting temperature 900 °C and reaction time 2 h (Zhang et al., 2016; Li et al., 2012). Although the fusion pretreatment with NaOH is successful for improving REE recovery from the waste phosphor in laboratory, it may not be preferred in industrial application, because it is expensive and highly corrosive to facilities especially in a fusion state and is very prone to deliquescing.

Na_2CO_3 assisted roasting is a practical means used to decompose REE phosphate and fluoro-carbonate minerals prior to REE solubilization by acid leaching (Kumari et al., 2015; Burgess et al., 2018), because Na_2CO_3, though less effective, is more acceptable from the technological and economic benefits. However, knowledge and understanding on the decomposition behavior and reaction mechanism of $CeMgAl_{11}O_{19}:Tb^{3+}$ with Na_2CO_3 during the roasting process are very limited so far. In the present work, the thermal decomposition behavior, phase evolution, valence states and microstructure changes for the $CeMgAl_{11}O_{19}:Tb^{3+}$ phosphor roasted with Na_2CO_3 were examined in detail through theoretical analysis and experimental investigation, with the focus on the fundamental understanding of the decomposition

mechanisms. In addition, the operating conditions including roasting temperature, the mass ratio of green phosphor to Na_2CO_3, and roasting time were systematically studied and optimized. The present research is expected to provide theoretical and technical knowledge on the effective extraction of REEs from waste phosphors, as well as Na_2CO_3 assisted decomposition of spinel-type solid wastes.

2. Experimental

2.1. Materials

The green phosphor powder with an average particle size of 2–5 μm used in this study was purchased from Shenzhen Obset Technology Ltd. (China). Its chemical composition measured with X-ray fluorescence analysis (XRF, ARLAdvant'X Intellipower™ 3600, Thermo Fisher, America) is listed in Table 1. The phase composition of the powder, analyzed with X-ray diffraction (XRD, D8 ADVANCE, BRUKER AXS), is presented in Fig. 1, indicating that it is composed mainly of $Ce_{0.67}Tb_{0.33}MgAl_{11}O_{19}$ and a portion of α-Al_2O_3. Generally, excessive Al_2O_3 is used in synthesizing the green phosphor to improve the reaction activity and reduce the consumption of terbium oxide, and thus Al_2O_3 is inevitably contained in the green phosphor (Tang et al., 2006; Liu et al., 2017). Na_2CO_3 was of analytical grade and used for roasting directly without further purification.

2.2. Roasting experiments

In a typical roasting experiment, a given amount of green phosphor powder and Na_2CO_3 were evenly mixed by grinding. The mixture was then introduced into corundum crucible and heated to the desired temperature in a muffle furnace under an air atmosphere with the heating rate of 10 °C·min^{-1}. After roasting for a certain time, the mixture was cooled gradually to room temperature inside the furnace. Subsequently, the product was dissolved in deionized water and filtered. Finally, the solid residual was washed with deionized water several times and dried in a vacuum oven. A series of roasting experiments were performed to get an optimum roasting condition. The product obtained from the optimum roasting condition was directly
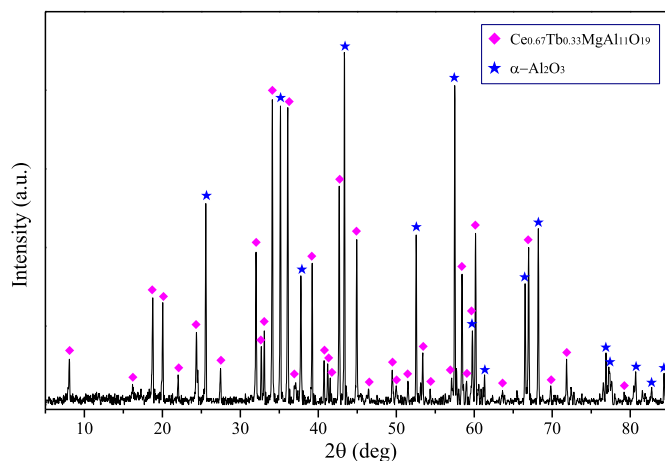
Fig. 1. X-ray diffraction pattern of green phosphor. (For interpretation of the references to color in this figure legend, the reader is referred to the Web version of this article.)

subjected to X-ray diffraction analysis without dissolving and washing.

2.3. Characterization

The composition of green phosphor and filter residue were analyzed by XRF. Thermal gravimetric (TG) and differential scanning calorimetry (DSC) analyses were performed using a simultaneous TG-DSC instrument (Setsys Evolution 18/24 TGA-DTA/DSC-MS, Setaram, France) under an air flow of $30\,mL\,min^{-1}$. The analysis was conducted from room temperature to $1100\,°C$ with a constant heating rate of $10\,°C\,min^{-1}$. A mass spectrometer (MS, OmniStar GSD320, Pfeiffer) coupled to the thermal analyzer was adopted to detect the gas evolving from the mixture because of the decomposition. The mass signals of H_2O and CO_2 were continuously recorded during the heating process. The crystal structures of the green phosphor powder and the roasted samples were identified with XRD by using the monochromatic target of Cu Kα with the acceleration voltage and electrical current of $30\,kV$ and $10\,mA$, respectively. The measurements were conducted for 2θ angle between 5° and 85° with a step size of 0.02°. The morphology and the mean particle size of the samples were examined with scanning electron microscopy (SEM, SSX-550, Shinadzu Corporation) at an accelerating voltage of $15\,kV$. An energy dispersive X-ray spectroscopy (EDS) coupled with SEM was simultaneously used to analyze the element composition of the samples. The valence states of the main elements were characterized with an X-ray photoelectron spectroscopy (XPS, ESCALAB 250Xi, Thermo Fischer, America) using monochromatized Al Ka source operated at $200\,W$ with the passing energy/step of $40\,eV/0.1\,eV$ for narrow scans. During the XPS measurements, the pressure in the main chamber was maintained below $8 \times 10^{-10}\,Pa$. All spectra were corrected by using the C 1s line at $284.6\,eV$ as the standard. The concentrations of Ce and Tb in the filtrate were determined by using inductively coupled plasma-atomicemission spectrometry (ICP-AES, ICPS-7510, Shimadzu, Japan). The leaching efficiency (η_i) was calculated according to Eq. (1):

$$\eta_i = \frac{c_i V}{w_i m} \tag{1}$$

where i is Ce or Tb, c_i is the concentration of element i in the filtrate (g L^{-1}), V represents the volume of the leachate (L), w_i is the mass fraction of element i in the original green phosphor, and m denotes the mass of green phosphor used in the leaching experiment (g).

3. Results and discussion

3.1. Thermodynamic analysis

In order to predict thermodynamically the reaction behavior of the green phosphor during Na_2CO_3 assisted roasting, the reaction equilibrium was calculated using the equilibrium module of the FactSage, a commonly used thermodynamic software based on the principle of Gibbs free energy minimization (Yu et al., 2016). Considering that $Ce_{0.67}Tb_{0.33}MgAl_{11}O_{19}$ is also in magnesia–alumina spinel structures (Wu et al., 2014), the thermodynamic data of spinel $MgAl_2O_4$ have been selected instead for equilibrium calculation because the data for $Ce_{0.67}Tb_{0.33}MgAl_{11}O_{19}$ are still lacking in the database of FactSage 7.2. The effect of temperature on the equilibrium compositions of the phases was simulated with an initial reaction mixture of $50.g\ Na_2CO_3$ and $50.0\ g\ MgAl_2O_4$ in a closed system, and the predicted results in the temperature range 500–1200 °C are present in Fig. 2. It can be seen that the spinel phase $MgAl_2O_4$ reacts with Na_2CO_3 at ~940 °C and generates $NaAlO_2$, MgO and CO_2. Thus, the phase evolution of magnesia–alumina spinel in Na_2CO_3 assisted roasting can be represented as follows:

$$MgAl_2O_4 + Na_2CO_3 \rightarrow 2NaAlO_2 + MgO + CO_2(g) \tag{2}$$
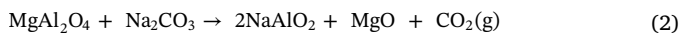
It is noteworthy that the equilibrium calculations were made in a closed system assuming the total pressure of 1.0 atm. Therefore, the
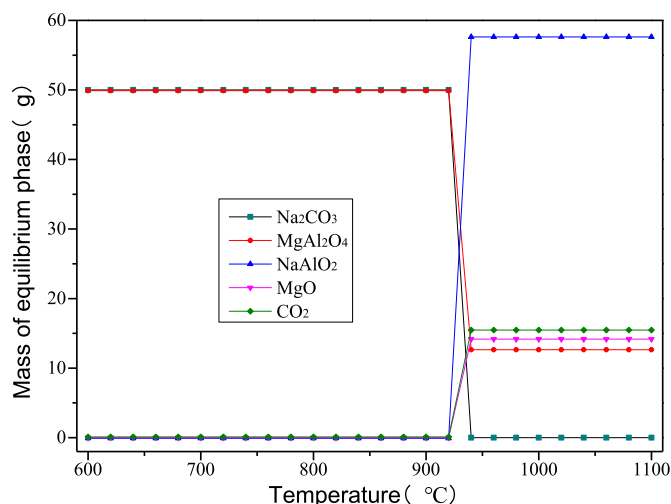
Fig. 2. Prediction of the equilibrium compositions for the system of 50 g $MgAl_2O_4$ + 50 g Al_2O_3 at 1 atm total pressure by using FactSage.

partial pressure of CO_2 is approximately equal to 1.0 atm in calculation because only CO_2 gas is generated during the reaction. Nevertheless, CO_2 partial pressure is fairly low as the gas is prone to flow away from the reaction products. Consequently, the temperature dependence of Gibbs free energy variation under different partial pressure of CO_2 is calculated using the reaction module of FactSage, as shown in Fig. 3. It indicates that when roasting temperature is over 930 °C, the change in standard Gibbs free energy given by Eq. (2) is negative. However, with the partial pressure of CO_2 decreases gradually, the temperature threshold for the onset of the decomposition is lowered. When the partial pressure of CO_2 decreases to 0.1 atm, the reaction can take place at about 630 °C. Based on the above analyses, it is theoretically feasible to decompose spinel aluminate to $NaAlO_2$ and MgO by Na_2CO_3 assisted roasting at a relatively lower temperature. It should be noted that the reaction behavior of the REEs in $Ce_{0.67}Tb_{0.33}MgAl_{11}O_{19}$ is still uncertain with thermodynamic calculations, due to the missing data. The results could only be used as a rough reference and will be refined in the future once the thermodynamic data for $Ce_{0.67}Tb_{0.33}MgAl_{11}O_{19}$ is available in the FactSage. Therefore, the accurate reaction behavior of $Ce_{0.67}Tb_{0.33}MgAl_{11}O_{19}$ should be further investigated through a series of experiments.
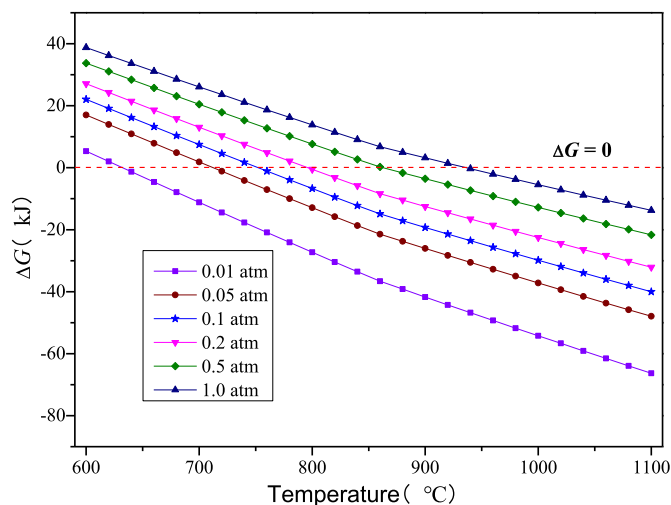
Fig. 3. Gibbs free energy variation of the reaction described in Eq. (2) under different CO_2 partial pressure (total pressure = 1 atm).
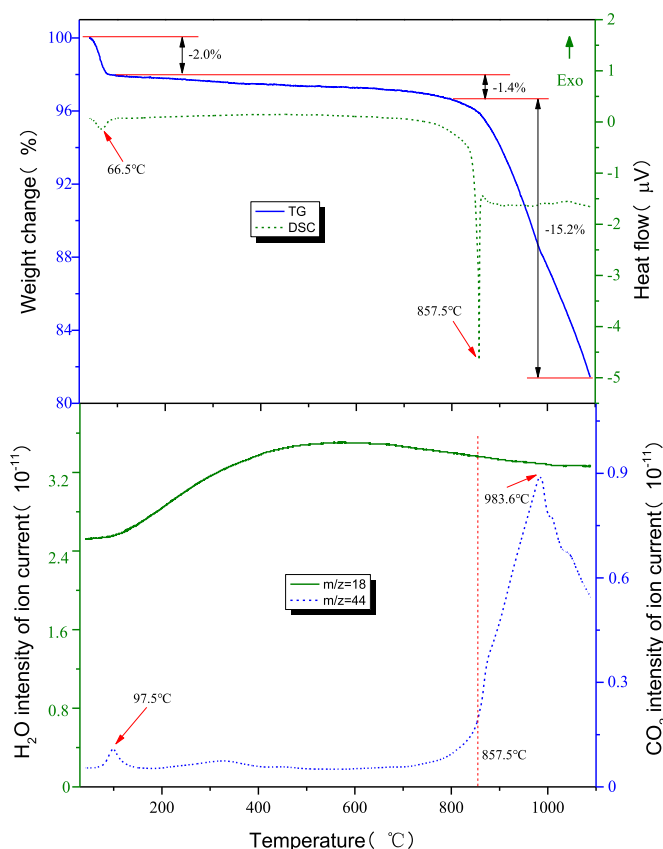
Fig. 4. TG-DSC/MS curves of the mixture of the green phosphor and Na_2CO_3 (mass ratio = 1:1). (For interpretation of the references to color in this figure legend, the reader is referred to the Web version of this article.)

3.2. Thermal decomposition behavior

The thermal decomposition behavior of the green phosphor in the presence of Na_2CO_3 was examined by using TG-DSC-MS analyses. A sample of 10.5 mg mixture of the green phosphor and Na_2CO_3 with a mass ration of 1:1 was taken for the test. As shown by the TG-DSC-MS curves in Fig. 4, the whole process could be generally divided into three stages. In the first stage, an obvious weight loss of approximately 2.0% occurred from room temperature to 100 °C, and an endothermic peak appeared in the DSC curve at around 66 °C. Meanwhile, the ionic strength values of H_2O and CO_2 were continuously increasing in the MS curves. It was reported that CO_2 could be captured by Na_2CO_3 to form $NaHCO_3$ and $Na_5H_3(CO_3)_4$ in the presence of water vapor at around 60 °C under atmospheric pressure via the following reactions (Liang, 2003; Liang et al., 2004), respectively.

$$Na_2CO_3(s) + CO_2(g) + H_2O(g) \rightleftharpoons 2NaHCO_3(s) \tag{3}$$

$$5Na_2CO_3(s) + 3CO_2(g) + 3H_2O(g) \rightleftharpoons 2Na_5H_3(CO_3)_4(s) \tag{4}$$
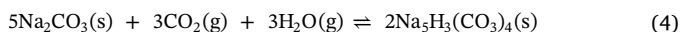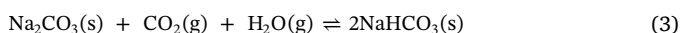
The above reactions are exothermic and thus a lower temperature is favorable (Luo and Kanoh, 2017). While heating, the reactions will proceed in the reverse direction with the release of H_2O and CO_2 gases. Therefore, except for the dehydration of physically absorbed water, the weight loss below 100 °C was also associated with the gas release resulting from the reversed reactions of Eqs. (3) and (4). The second stage, within a large temperature region of 100–800 °C, showed a very slow weight loss in the TG curve, and this was resulted from the removal of chemically-bound water in the mixture, which could be confirmed by the MS curve that the ionic strength values of H_2O was gradually increasing. When the temperature was raised to 800 °C, the roasting process proceeded into the last stage. At the beginning of this

stage, a moderate weight loss appeared in the TG curve, and the ionic intensity of CO_2 in the MS curve increased simultaneously, indicating that the green phosphor started to react with solid Na_2CO_3 and CO_2 was evolved. As the temperature was further raised to 857.5 °C, a sudden weight loss accompanied by a rapid increasing of the ionic intensity of CO_2 occurred, corresponding to the sharp endothermic peak in the DSC curve. This is because solid Na_2CO_3 is transformed to liquid when the temperature rises up to 857.5 °C, which is close to its melting point of 851 °C. It is quite evident that molten Na_2CO_3 compared to solid Na_2CO_3, is more favorable for the decomposition of the green phosphor because of the better mixing and faster mass transfer. Therefore, the green phosphor was decomposed rapidly at temperatures over 857.5 °C, resulting in a significant weight loss and CO_2 release. The ionic intensity of CO_2 reached a maximum value at 983.6 °C, which suggested that the decomposition process was slowed down above this temperature due to the intensive depletion of the reactants after the reaction lasted for a period of time.

3.3. Phase evolution during roasting

In order to reveal the phase evolution during roasting, large scale roasting experiment were conducted, and the roasting products under various conditions were characterized with XRD after washing in deionized water (see Fig. 5). The XRD patterns of the roasted products at different temperatures for 3 h with a mass of the green phosphor to Na_2CO_3 = 1:2 are depicted in Fig. 5a. After roasting at 800 °C, two weak characteristic diffraction peaks assigned to Tb_2O_3 and CeO_2 whose standard diffraction peaks are overlapped, appeared apart from the diffraction peaks of the original $Ce_{0.67}Tb_{0.33}MgAl_{11}O_{19}$ and α-Al_2O_3. It can be inferred that $Ce_{0.67}Tb_{0.33}MgAl_{11}O_{19}$ in the green phosphor starts to decompose by sintering with Na_2CO_3 at 800 °C via solid-solid reaction. It is worthy to note that MgO which should be generated during the decomposition process according to thermodynamic equilibrium calculations, has not been detected due to the low content of magnesium in the green phosphor and its relatively lower diffraction intensity compared to Tb_2O_3/CeO_2. When the temperature is raised to 850 °C, there are no obvious changes in the XRD patterns but another new weak diffraction peak ascribed to Tb_2O_3 and CeO_2 arises at 56.7°. $Ce_{0.67}Tb_{0.33}MgAl_{11}O_{19}$ can chemically react with solid Na_2CO_3 at 800–850 °C, but weakly and slowly. Further increasing temperature to 900 °C, Na_2CO_3 has melted to liquid, and thus the decomposition process is consequentially accelerated. As a result, the diffraction peaks of $Ce_{0.67}Tb_{0.33}MgAl_{11}O_{19}$ are evidently weakened whereas the diffraction intensities of Tb_2O_3 and CeO_2 distinctly increase. In addition, an un-apparent diffraction peak is detected at 62.3°, which is attributed to the formation of MgO phase. The diffraction intensities of Tb_2O_3 and CeO_2 remarkably increase and the formation of MgO is clearly evident with the temperature increases from 900 °C to 950 °C, meanwhile the peaks of $Ce_{0.67}Tb_{0.33}MgAl_{11}O_{19}$ begin to disappear, suggesting that the decomposition of $Ce_{0.67}Tb_{0.33}MgAl_{11}O_{19}$ is close to completion. While the temperature increases to 1000 °C, the diffraction peaks of MgO strengthen further, and the Tb_2O_3/CeO_2 peak intensities reach the maximum values whereas the diffraction peaks of $Ce_{0.67}Tb_{0.33}MgAl_{11}O_{19}$ disappear completely. Therefore, it is reasonable to conclude that the roasting temperature plays a significant role in decomposing the spinel structure of $Ce_{0.67}Tb_{0.33}MgAl_{11}O_{19}$. Higher temperature is beneficial for the decomposition of $Ce_{0.67}Tb_{0.33}MgAl_{11}O_{19}$ due to its positive effect on the mass transfer, which will be discussed in detail later. The above results are consistent with those of TG-DSC/MS analyses. Moreover, it can be seen in Fig. 5a, α-Al_2O_3 is a thermally stable phase throughout the whole roasting process, which implies that compared with Al_2O_3, $Ce_{0.67}Tb_{0.33}MgAl_{11}O_{19}$ is easier to be attacked by Na_2CO_3. The industrial soda-lime process for bauxite sintering generally uses a temperature above 1150 °C. However, a temperature of 1000 °C is enough to achieve the complete decomposition of $Ce_{0.67}Tb_{0.33}MgAl_{11}O_{19}$. This
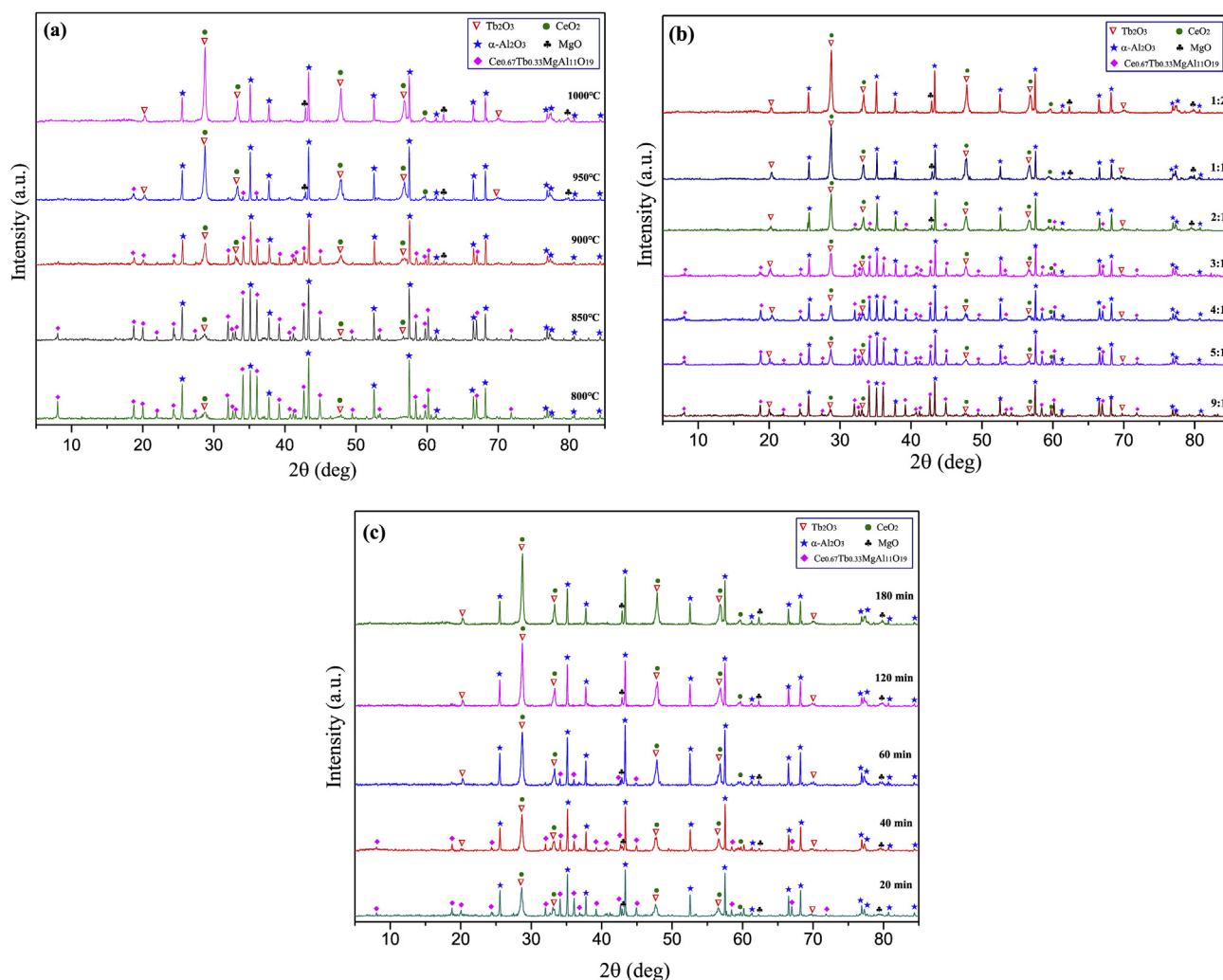
Fig. 5. XRD patterns of the roasted products after washing as a function of (a) roasting temperature, (b) mass ratio of the green phosphor/Na$_2$CO$_3$, and (c) holding time. (For interpretation of the references to color in this figure legend, the reader is referred to the Web version of this article.)

is undoubtedly beneficial for the extraction of valuable REEs from the waste phosphors. Based on the thermodynamics calculation and the TG-DSC/MS analyses, the decomposition process of Ce$_{0.67}$Tb$_{0.33}$MgAl$_{11}$O$_{19}$ during the Na$_2$CO$_3$ assisted roasting under air can be tentatively illustrated by Eq. (5).

$$Ce_{0.67}Tb_{0.33}MgAl_{11}O_{19} + Na_2CO_3 \xrightarrow{in\ air} CeO_2 + Tb_2O_3 + MgO$$
$$+ NaAlO_2 + CO_2(g) \qquad (5)$$
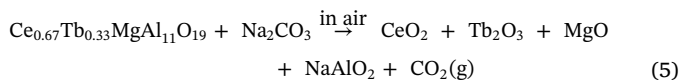
Fig. 5b presents the phase evolution of the green phosphor roasted with various dosages of Na$_2$CO$_3$ at 1000 °C for 3 h. When the mass ratio of green phosphor to Na$_2$CO$_3$ was 9:1, the roasted products after washing were still dominated by Ce$_{0.67}$Tb$_{0.33}$MgAl$_{11}$O$_{19}$ and α-Al$_2$O$_3$, with Tb$_2$O$_3$ and CeO$_2$ as minor phases. The Ce$_{0.67}$Tb$_{0.33}$MgAl$_{11}$O$_{19}$ diffraction peaks weaken gradually whereas the diffraction peaks of Tb$_2$O$_3$ and CeO$_2$ show the opposite variation trend with the increasing of Na$_2$CO$_3$ addition. As the mass ratio of the green phosphor to Na$_2$CO$_3$ turns to 2:1, the decomposition process proceeds to a great extent due to the amount of melted Na$_2$CO$_3$ is presumably enough to clad the Ce$_{0.67}$Tb$_{0.33}$MgAl$_{11}$O$_{19}$ particles during roasting. Thus, the diffraction peaks of Tb$_2$O$_3$ and CeO$_2$ further strengthen and the MgO phase is also observed, while the Ce$_{0.67}$Tb$_{0.33}$MgAl$_{11}$O$_{19}$ diffraction peaks almost disappear. Ce$_{0.67}$Tb$_{0.33}$MgAl$_{11}$O$_{19}$ was fully decomposed by roasting with an equivalent mass of Na$_2$CO$_3$. Further increasing the Na$_2$CO$_3$ dosage could not promote the decomposition process as there was no

apparent change in the XRD patterns.

Fig. 5c shows the XRD patterns of the mixture of the green phosphor and Na$_2$CO$_3$ (mass ratio = 1:2) roasted at 1000 °C for various holding time. It indicated that the diffraction peaks of Ce$_{0.67}$Tb$_{0.33}$MgAl$_{11}$O$_{19}$ gradually decrease with prolonging holding time from 20 to 60 min, and a holding time of 120 min is sufficient for the complete decomposition of Ce$_{0.67}$Tb$_{0.33}$MgAl$_{11}$O$_{19}$. Further increase of holding time does not result in distinct changes in phases. As mentioned above, α-Al$_2$O$_3$ is hardly attacked by Na$_2$CO$_3$ and still exists as a major phase in the products even under the rigorous roasting conditions. This is probably related to the fairly slow reaction between Al$_2$O$_3$ and Na$_2$CO$_3$, as illustrated by Eq. (6).

$$Al_2O_3 + Na_2CO_3 = 2NaAlO_2 + CO_2(g) \qquad (6)$$

It was found that the reaction would not finish in less than 7 h at roasting temperature of 1000 °C and 1 h even at 1150 °C (Bi, 2006). α-Al$_2$O$_3$ is the thermodynamically most stable phase among aluminum oxides, and the complete reaction of α-Al$_2$O$_3$ with Na$_2$CO$_3$ at 1000 °C may take a much longer time. Consequently, Ce$_{0.67}$Tb$_{0.33}$MgAl$_{11}$O$_{19}$ in the green phosphor has been completely decomposed by roasting with Na$_2$CO$_3$ at 1000 °C for 120 min, leaving a considerable amount of unreacted α-Al$_2$O$_3$ in the roasting product. When the holding time further extends to 180 min, the peak intensities of α-Al$_2$O$_3$ decrease compared to those of Tb$_2$O$_3$ and CeO$_2$. This finding, in turn, suggests that Ce$_{0.67}$Tb$_{0.33}$MgAl$_{11}$O$_{19}$ will be preferentially attacked by Na$_2$CO$_3$
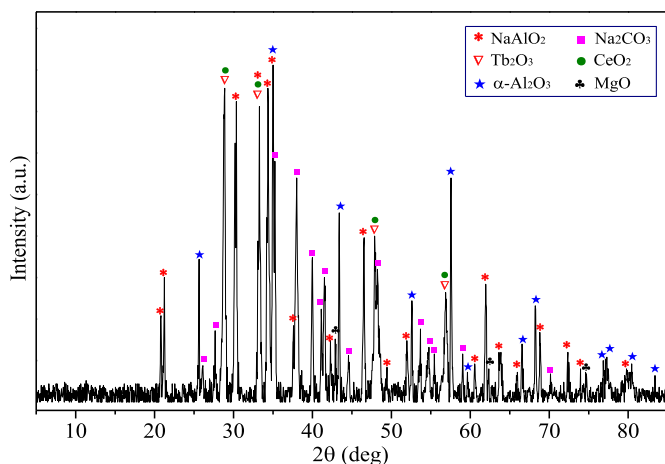
Fig. 6. XRD pattern of the mixture of the green phosphor/Na_2CO_3 (mass ratio = 1:1) roasted at 1000 °C for 2 h. (For interpretation of the references to color in this figure legend, the reader is referred to the Web version of this article.)

during roasting.

Therefore, aimed at recovery of valuable Ce and Tb, a temperature of 1000 °C, a mass ratio of the green phosphor to Na_2CO_3 = 1:1, and a holding time of 120 min is the appropriate roasting condition based on the consideration of saving energy and reducing Na_2CO_3 consumption. The XRD pattern of the roasted product is shown in Fig. 6. The diffraction peaks of $Ce_{0.67}Tb_{0.33}MgAl_{11}O_{19}$ are not found, while the phases of CeO_2, Tb_2O_3, MgO and $NaAlO_2$ are present in the product. Meanwhile, α-Al_2O_3 and Na_2CO_3 still coexist in the product after roasting. It is further confirmed that $Ce_{0.67}Tb_{0.33}MgAl_{11}O_{19}$ preferentially reacts with Na_2CO_3 and has been completely converted to CeO_2, Tb_2O_3, MgO and $NaAlO_2$ under this roasting condition. To more accurately determine the effect of Na_2CO_3 assisted roasting on the decomposition of $Ce_{0.67}Tb_{0.33}MgAl_{11}O_{19}$, the above roasted product was firstly washed with deionized water to remove the soluble substances, and then leached in hot HCl-H_2O_2 solution. The leaching efficiencies of both Ce and Tb are above 98% (see Table 2). It is indicated that the REEs in green phosphor have almost fully converted to REE oxides after roasting.

3.4. Valence states change

XPS measurements are conducted to further investigate the surface chemical bonding and the chemical valence state of constituent elements in the original green phosphor and the roasted product with equivalent mass of Na_2CO_3 at 1000 °C for 120 min under air after washing, and the results are shown in Fig. 7. The full-scale XPS survey in Fig. 7a proves the presence of Ce, Tb, Al, Mg and O elements both in the original green phosphor and in the roasted sample according to the specific binding energy values calibrated by the C 1s standard spectrum (284.60 eV). However, two peaks assigned to Na are also present in the XPS pattern of the roasted sample, likely originated from the excessive Na_2CO_3 or the generated $NaAlO_2$ which has not been washed off completely by deionized water. Moreover, the narrow sweeping for Al2p, Ce3d, Tb3d and Mg1s of the XPS spectra are shown in Fig. 7b–e to reveal their chemical bonding changes and valence state variations

during roasting. As mentioned previously, the component Al mainly exists in the form of α-Al_2O_3 both in the original phosphor and in the roasted sample after washing. It can be seen from Fig. 7b that for both the original phosphor and the roasted sample, the binding energy peaks of Al2p are immutably located in 73.8 eV, which is the characteristic of the Al in α-Al_2O_3 (Slavinskaya et al., 2004). Comparing the Al2p spectra before and after roasting, it is clear that the peak area reduces, because Al in the phosphor partly transforms into the soluble $NaAlO_2$ during Na_2CO_3 assisted roasting and has been removed by washing. The binding energy values of Ce3d for the original phosphor are 885.3 and 903.8 eV (shown in Fig. 7c), and correspond to energy level of $Ce3d_{5/2}$ and $Ce3d_{3/2}$ of Ce^{3+}, respectively, which are the characteristics of Ce element associated with Tb in the compound $Ce_{0.9}Tb_{0.1}PO_4$ (Pemba-Mabiala et al., 1990). After roasting with Na_2CO_3 under air, four Ce3d binding energy peaks are present in the sample. The peaks at approximately 881.2, 888.1 and 899.6 eV are attributed to $Ce3d_{5/2}$ for Ce^{4+} valence state, and the peak at 897.2 eV is ascribed to $Ce3d_{3/2}$ for Ce^{4+} valence state. The results are in good agreement with that of pure CeO_2 (Wu et al., 2016; Sarkar et al., 2014; Xiu et al., 2018). It means that the Ce^{3+} in the green phosphor has been oxidized to Ce^{4+} and transformed to pure CeO_2 during the roasting process. The oxidization is likely resulted from the oxygen in air. Therefore, the decomposition reaction represented in Eq. (5) can be more accurately expressed as follows.

$$2Ce_{0.67}Tb_{0.33}MgAl_{11}O_{19} + 11Na_2CO_3 + \frac{1}{3}O_2 \rightarrow \frac{4}{3}CeO_2 + \frac{1}{3}Tb_2O_3$$
$$+ 2MgO + 22NaAlO_2 + 11CO_2(g) \quad (7)$$
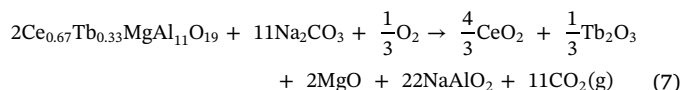
The spectra of Tb3d are shown in Fig. 7d. For the original phosphor, the binding energy values of 1242.2 and 1277.1 eV representing the energy level of $Tb3d_{5/2}$ and $Tb3d_{3/2}$, correspond to those of Tb^{3+} in the $Ce_{0.9}Tb_{0.1}PO_4$ (Pemba-Mabiala et al., 1990), which matches well with the binding energy peak positions of Ce3d depicted in Fig. 7c. After roasting with Na_2CO_3, the $Tb3d_{5/2}$ and $Tb3d_{3/2}$ binding energy peaks shift to 1241.0 and 1277.0 eV, respectively, which are consistent with that of pure Tb_2O_3 (Zhang et al., 2017). As for Mg, no evident peaks corresponding to Mg1s can be observed in the original sample, as shown in Fig. 7d. Although this is partly due to the fairly low content of Mg in the green phosphor, the main reason is that Mg atoms are located in the interior of $Ce_{0.67}Tb_{0.33}MgAl_{11}O_{19}$ spinel (Liu et al., 2017) and are hardly detected by XPS. However, in the roasted sample, Mg exists in the form of MgO and distributes on the surface of the crystals. Therefore, a high Mg1s peak centered at 1304.1 eV has been detected in the XPS spectrum, which is a characteristic of Mg element in MgO (Cui et al., 2018). Based on the above analyses, it can be further confirmed that $Ce_{0.67}Tb_{0.33}MgAl_{11}O_{19}$ in the green phosphor has been completely decomposed to form CeO_2, Tb_2O_3 and MgO by roasting, while most of Al_2O_3 is still free of Na_2CO_3 attacking and maintains its original state. That is quite consistent with the aforementioned fact that in comparison with Al_2O_3, $Ce_{0.67}Tb_{0.33}MgAl_{11}O_{19}$ is more liable to be attacked by Na_2CO_3 during roasting.

3.5. Micromorphology variations

Microstructure and microzone chemical composition of the green phosphor and the roasted products after washing were analyzed with SEM/EDS to clarify the morphological variations during roasting. As

Table 2
Leaching efficiency of REEs from green phosphor pretreated by Na_2CO_3 assisted roasting.

Leaching conditions					Leaching efficiency (%)	
Concentration of HCl (mol L^{-1})	Concentration of H_2O_2 (g L^{-1})	Temperature (°C)	Time (h)	Liquid/solid ratio (mL g^{-1})	Ce	Tb
5.0	4.5	70	3.0	50	98.4	99.2
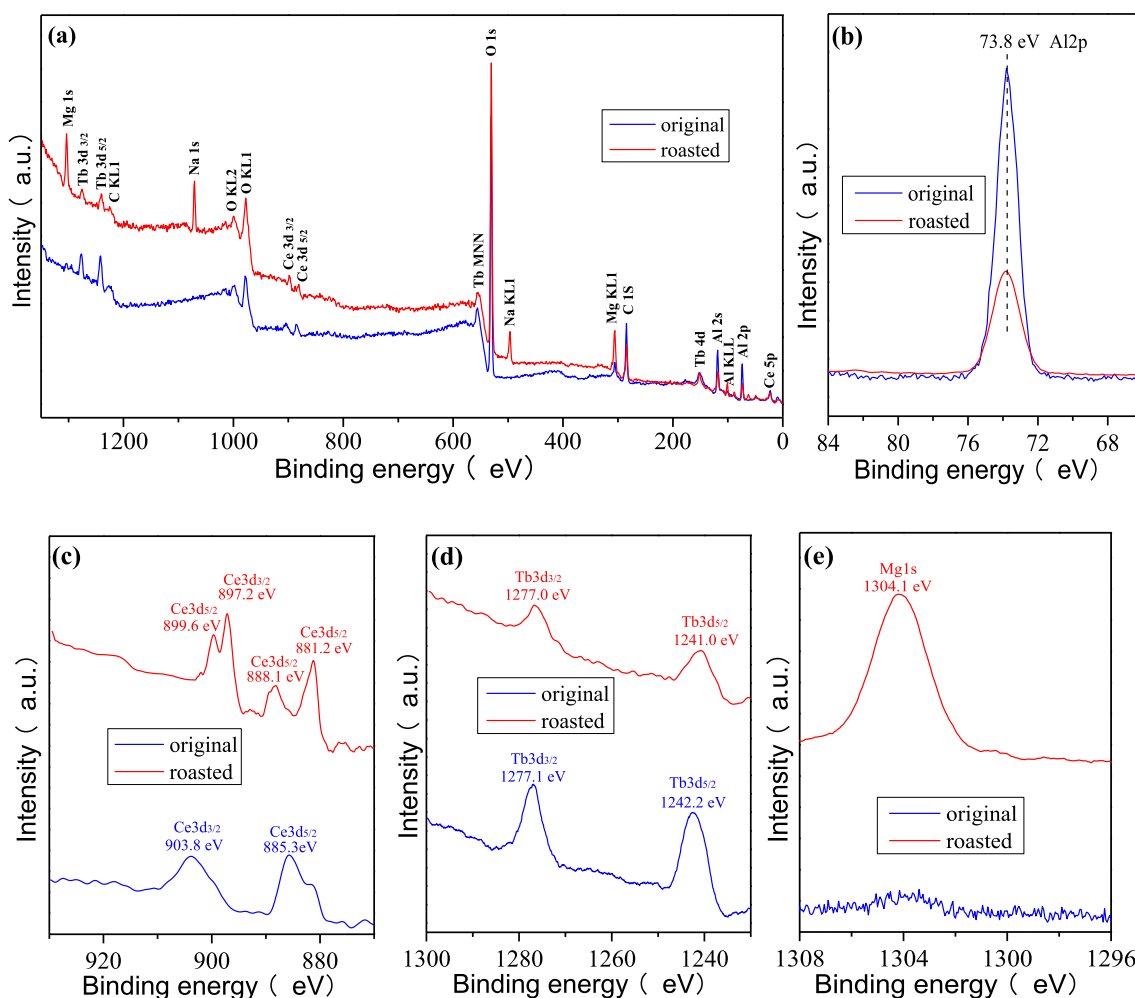
Fig. 7. XPS spectra of the original and the sample roasted with equivalent mass of Na_2CO_3 at 1000 °C for 120min under air. (a) survey; (b) Al 2p; (c) Ce 3d; (d) Tb 3d; (e) Mg 1s.

shown in Fig. 8a, the original phosphor is composed of irregular sphere-like granules with an average diameter of 2–5 μm. The EDS results indicate that $Ce_{0.67}Tb_{0.33}MgAl_{11}O_{19}$ mainly exists in the smaller granules of about 3 μm while the larger granules are α-Al_2O_3. Conventionally, green phosphor are synthesized via solid-state reaction method above 1600 °C using the corresponding oxides as the starting materials (Feng et al., 2010), and usually excessive Al_2O_3 is added (Tang et al., 2006). The large granules probably result from the fast grain growth of Al_2O_3 during high temperature roasting. After roasting with Na_2CO_3 at 900 °C, the glossy surface becomes rough and some tiny particles are generated, however the granules are unbroken and still keep their initial outline, as seen in Fig. 8b. Increasing the roasting temperature to 1000 °C, the $Ce_{0.67}Tb_{0.33}MgAl_{11}O_{19}$ granules has been decomposed almost completely to numerous fine particles, which are severely agglomerated together. From the EDS spectrum of point c-1 in Fig. 8c, it can be seen that the contents of Ce and Tb in the generated particles increase obviously, while the case of Al is on the contrary. It suggests that the roasting temperature is the critical factor to the decomposition of $Ce_{0.67}Tb_{0.33}MgAl_{11}O_{19}$, and the element Al from disintegrated $Ce_{0.67}Tb_{0.33}MgAl_{11}O_{19}$ has converted to a water soluble substance $NaAlO_2$ that can be removed by washing. It is obvious to note that some large granules of Al_2O_3, confirmed by EDS analyses (see spectra of point b-2 and c-2 in Fig. 8b and c), are persistently present in the products after roasting. The results convincingly validate the conclusion drawn previously that compared with $Ce_{0.67}Tb_{0.33}MgAl_{11}O_{19}$, Al_2O_3 is much more difficult to be attacked by Na_2CO_3 during the roasting process.

3.6. Role of Na_2CO_3 in decomposition

Fig. 9 shows the macroscopic features of the mixtures of the green phosphor and Na_2CO_3 before and after roasting. There is an apparent color change in the roasted mixtures. After roasting at 1000 °C for 2 h, the whole mixtures show a pale yellow color, which can be attributed to the formation of cerium oxide (Sun et al., 2004). This indicates that $Ce_{0.67}Tb_{0.33}MgAl_{11}O_{19}$ reacts completely because no white particles have been found in the roasted mixtures. Meanwhile, many small voids are formed on the surface of the roasted sample, which can be clearly seen from the enlarged picture in Fig. 9b. Moreover, it can be seen that the mixture mound is expanded slightly during roasting, indicating that a large number of voids are also formed inside the roasted mixtures. For the original mixtures, macroscopic voids could not be formed among the mineral particles due to their extremely small grain size. Undoubtedly, the voids are mainly derived from the depletion of Na_2CO_3 and the synchronous formation of CO_2 gas in reaction. In addition, although the mixtures have been roasted into a whole block, it does not adhere to the corundum boat at all and can be easily taken out. Interestingly, the roasted block is naturally loosed into particles by soaking in water at room temperature. This characteristic is beneficial for the subsequent REE extraction.

In fact, the decomposition of $Ce_{0.67}Tb_{0.33}MgAl_{11}O_{19}$ during Na_2CO_3 assisted roasting is a three-phase (solid aluminates and oxides, liquid Na_2CO_3 and gaseous CO_2) reaction. At 1000 °C, the particles of Na_2CO_3 turn to liquid droplets and will rest on the exterior surface of the solid
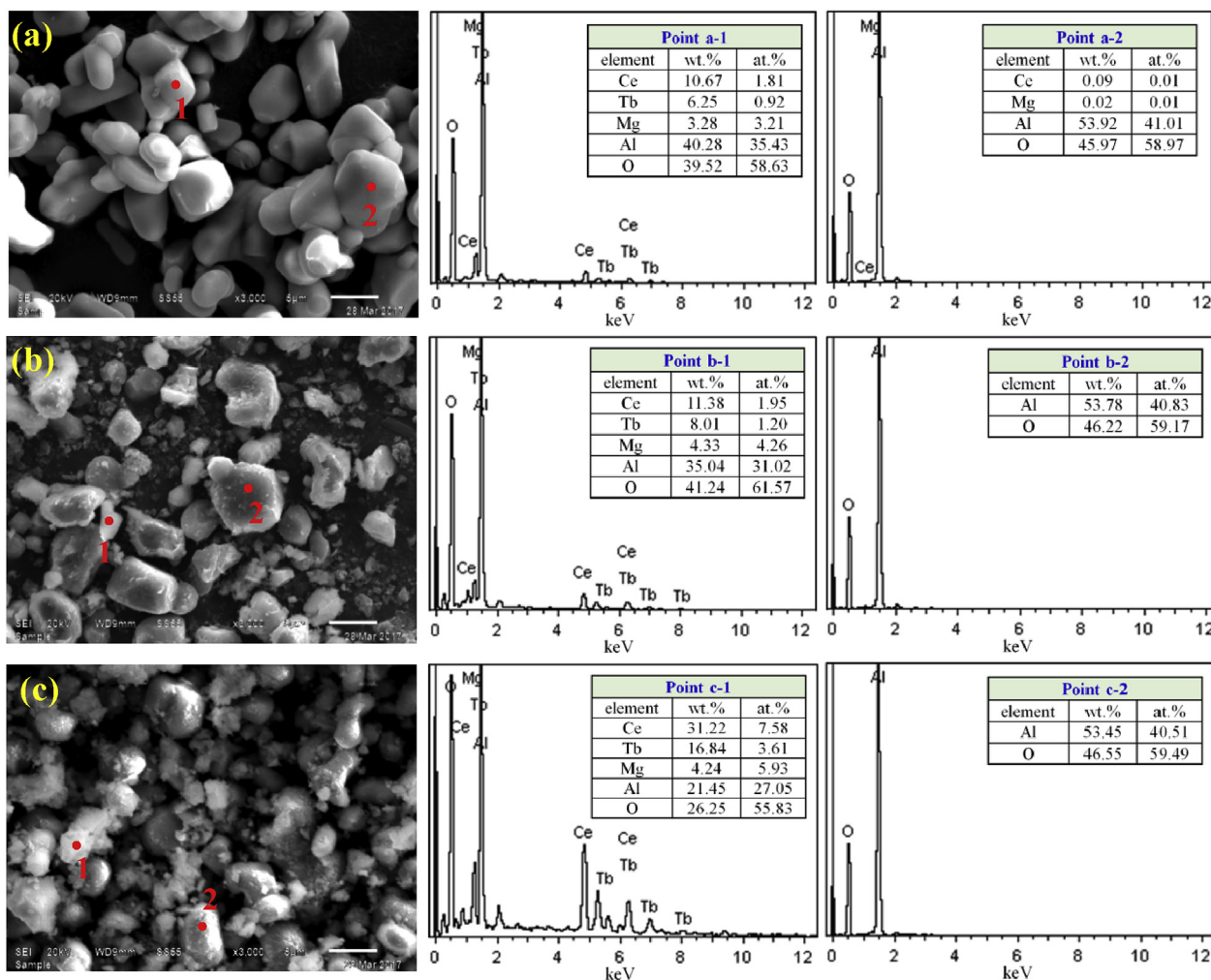
Fig. 8. SEM images and EDS spectra of original green phosphor (a) and the sample roasted with equivalent mass of Na_2CO_3 at 900 °C (b) and 1000 °C (c) for 60min under air. (For interpretation of the references to color in this figure legend, the reader is referred to the Web version of this article.)
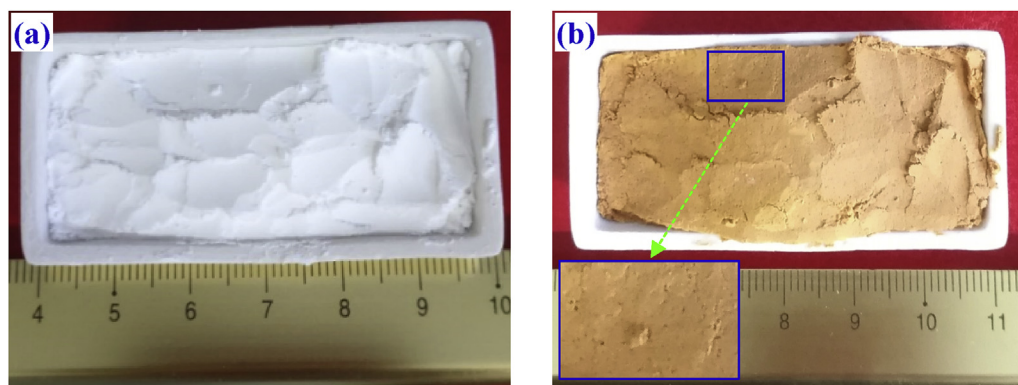
Fig. 9. Photos of the mixture of the original green phosphor and Na_2CO_3 with a mass ratio = 1:1 (a) and the mixture roasted at 1000 °C for 2 h (b). (For interpretation of the references to color in this figure legend, the reader is referred to the Web version of this article.)

$Ce_{0.67}Tb_{0.33}MgAl_{11}O_{19}$. These small Na_2CO_3 droplets cannot aggregate together and sink down under gravity because they are isolated by the closed voids. Once the $Ce_{0.67}Tb_{0.33}MgAl_{11}O_{19}$ particles come into contact with liquid Na_2CO_3, the reaction would take place. Na_2CO_3 droplets are gradually consumed until the compete decomposition of $Ce_{0.67}Tb_{0.33}MgAl_{11}O_{19}$. Along with the decomposition reaction, some voids will form spontaneously, and thus facilitate the transportation of liquid Na_2CO_3 and gaseous CO_2 in the partially roasted mixtures, which

could accelerate the decomposition of the unreacted $Ce_{0.67}Tb_{0.33}MgAl_{11}O_{19}$ illustrated in Eq. (5). In the porous roasted block, the transfer rate v ($m^2 s^{-1}$) of liquid Na_2CO_3 is inversely proportional to its dynamic viscosity η (Pa s), as represented in Eq. (8) (Lu and Likos, 2004).

$$v = -C\frac{d^2\rho g}{\eta}\nabla h$$

(8)

8

where C is a dimensionless constant related to the pore geometry, d corresponds to the pore diameter (m), ρ designates the density of the liquid Na_2CO_3 (kg m^{-3}), g is the acceleration of gravity (9.8 m s^{-2}), ∇h denotes the driver gradient (m). However, the viscosity of liquid Na_2CO_3 has a relationship with temperature T (K), and can be approximately expressed with the following Arrhenius-type equation in the temperature range of 875–1000 °C (Janz and Saegusa, 1963).

$$\eta = A e^{\frac{E}{RT}} \tag{9}$$

where A is the pre-exponential constant, E represents the activation energy for viscous flow (J mol^{-1}), and R is the molar gas constant (8.314 J mol^{-1} K^{-1}). It means that the transfer rate of Na_2CO_3 is increased with increasing the roasting temperature because the values of A and E in Eq. (9) are positive. On the other hand, it is reported that the minimum pore diameter d_{min} (m) in the roasted product required for the entrance of a molten droplet can be estimated using the following equation (Ji et al., 2017).

$$d_{min} = \frac{4(\sigma_{sl} - \sigma_{sg})}{P_0} \tag{10}$$

where P_0 is the external pressure withstood by liquid Na_2CO_3 at the interface between solid $Ce_{0.67}Tb_{0.33}MgAl_{11}O_{19}$ and liquid Na_2CO_3 (Pa), σ_{sl} and σ_{sg} represent the interfacial tensions between solid $Ce_{0.67}Tb_{0.33}MgAl_{11}O_{19}$ and liquid Na_2CO_3 and between solid $Ce_{0.67}Tb_{0.33}MgAl_{11}O_{19}$ and air (N m^{-1}), respectively. Both P_0 and σ_{sg} can be considered as constants, while σ_{sl} decreases with increasing of the temperature. Therefore, liquid Na_2CO_3 can transfer through a smaller channel at a higher temperature. It implies that at 1000 °C, liquid Na_2CO_3 is more readily to diffuse to the inner core of the unreacted $Ce_{0.67}Tb_{0.33}MgAl_{11}O_{19}$ carrying the reaction forward. In summary, at a higher roasting temperature of 1000 °C, the relatively lower viscosity and smaller required pore diameter are mainly responsible for the effortless transfer of liquid Na_2CO_3 inside the mixtures and accordingly realize the complete decomposition of $Ce_{0.67}Tb_{0.33}MgAl_{11}O_{19}$. This viewpoint has been verified by Ji et al. in extracting vanadium from vanadium slag via NaOH assisted roasting (Ji et al., 2017).

3.7. Decomposition mechanism

The SEM images shown in Fig. 8 indicate that the $Ce_{0.67}Tb_{0.33}MgAl_{11}O_{19}$ particles decompose gradually from the surface toward the core during roasting. Therefore, it is reasonable to draw the decomposition mechanism of $Ce_{0.67}Tb_{0.33}MgAl_{11}O_{19}$ in the Na_2CO_3 assisted roasting with the unreacted shrinking core model (Hua et al., 2014). The whole decomposition process can be divided into several steps occurring successively, and the schematic diagram is depicted in Fig. 10.

(1) As the roasting temperature increases above 851 °C, Na_2CO_3 will melt to ionic liquid and transports to the surface of the $Ce_{0.67}Tb_{0.33}MgAl_{11}O_{19}$ particles.

(2) The reaction takes place on the surface of the particles, and thus the surface becomes rougher due to the formation of cracks and small pores.

(3) The outer layer of $Ce_{0.67}Tb_{0.33}MgAl_{11}O_{19}$ breaks into small particles after a period of reaction and the products diffuse outward to the surrounding liquid phase to form a product layer.

(4) The reaction interface is moving gradually toward the core of unreacted $Ce_{0.67}Tb_{0.33}MgAl_{11}O_{19}$. Consequently, the product layer grows thicker and the unreacted core becomes smaller until the complete decomposition of $Ce_{0.67}Tb_{0.33}MgAl_{11}O_{19}$. As a result, the $Ce_{0.67}Tb_{0.33}MgAl_{11}O_{19}$ will fully decompose to smaller particles, which may aggregate together in the liquid phase.

The unreacted shrinking core model assumes that the volume change rate of the unreacted core is proportional to its surface area (Rajak et al., 2016). For a spherical particle, the conversion rate (α) varies regularly with reaction time (t) at a constant reaction rate (k) as expressed in Eq. (11) (Liu et al., 2017).

$$\alpha = 1 - [1 - (k/r_0)t]^3 \tag{11}$$

where r_0 is the initial radius of the particle (m). The $Ce_{0.67}Tb_{0.33}MgAl_{11}O_{19}$ particles in the present study can be approximately regarded as spheres of 3 μm on average. As shown in Fig. 5, at 1000 °C the complete decomposition of $Ce_{0.67}Tb_{0.33}MgAl_{11}O_{19}$ can be finished in 2 h. Thereby, the reaction rate constant is calculated as 4.2×10^{-10} m s^{-1} by substituting $\alpha = 1$, $r_0 = 3 \times 10^{-6}$ and $t = 7.2 \times 10^3$ into Eq. (11). This value of the reaction rate constant qualitatively indicates that the decomposition rate of $Ce_{0.67}Tb_{0.33}MgAl_{11}O_{19}$ in liquid Na_2CO_3 will be at nanometers per second.

Particularly, according to the experimental investigations, the structural decomposition of aluminate $Ce_{0.67}Tb_{0.33}MgAl_{11}O_{19}$ during the roasting process can be explained by the cation-oxoanion synergies theory (Liu et al., 2017). When Na_2CO_3 melts to liquid, the cations Na$^+$ and oxoanions CO_3^{2-} in the liquid are free to move. Therefore, Ce^{3+} and Tb^{3+} ions on the mirror plane in the spinel structure will be substituted by Na$^+$ because of their approximate equivalent ion radiuses, and then bond with the oxoanions CO_3^{2-}. The combination of two ionic forces makes REE ions escape from the crystal structure and subsequently convert to CeO_2, Tb_2O_3 and CO_2. Nevertheless, the substitution would cause more interstitial ions and oxygen vacancies around the sodium ion sites, and thus resulted in lattice distortion. Consequently, the neighboring ions of O^{2-}, Al^{3+} and Na$^+$ regroup to $NaAlO_2$ in the spinel blocks, while Mg^{2+} ions will bond with CO_3^{2-} to generate MgO and CO_2. The synergistic effect of cation-oxoanion ensures that simple CeO_2 and Tb_2O_3 can be extracted from the green phosphor via Na_2CO_3 assisted roasting technology.

3.8. Complete recycling route for waste phosphor

Based on the above investigations and the chemical composition of
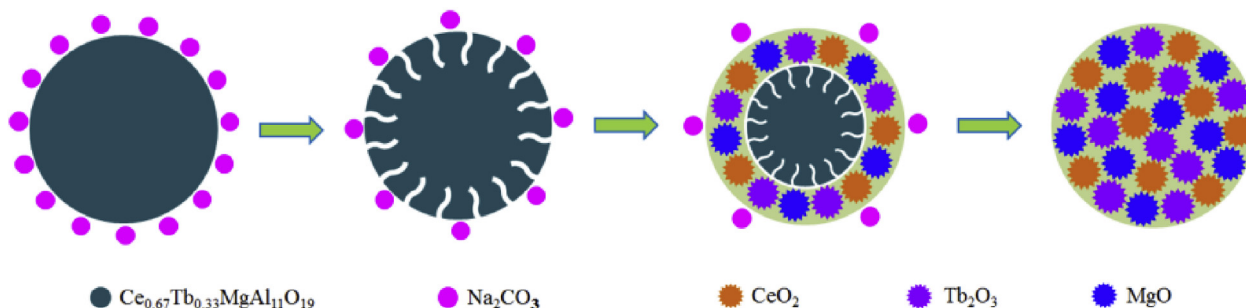
Fig. 10. Schematic representation of the probable decomposition mechanism during roasting.

Legend: $Ce_{0.67}Tb_{0.33}MgAl_{11}O_{19}$ — Na_2CO_3 — CeO_2 — Tb_2O_3 — MgO
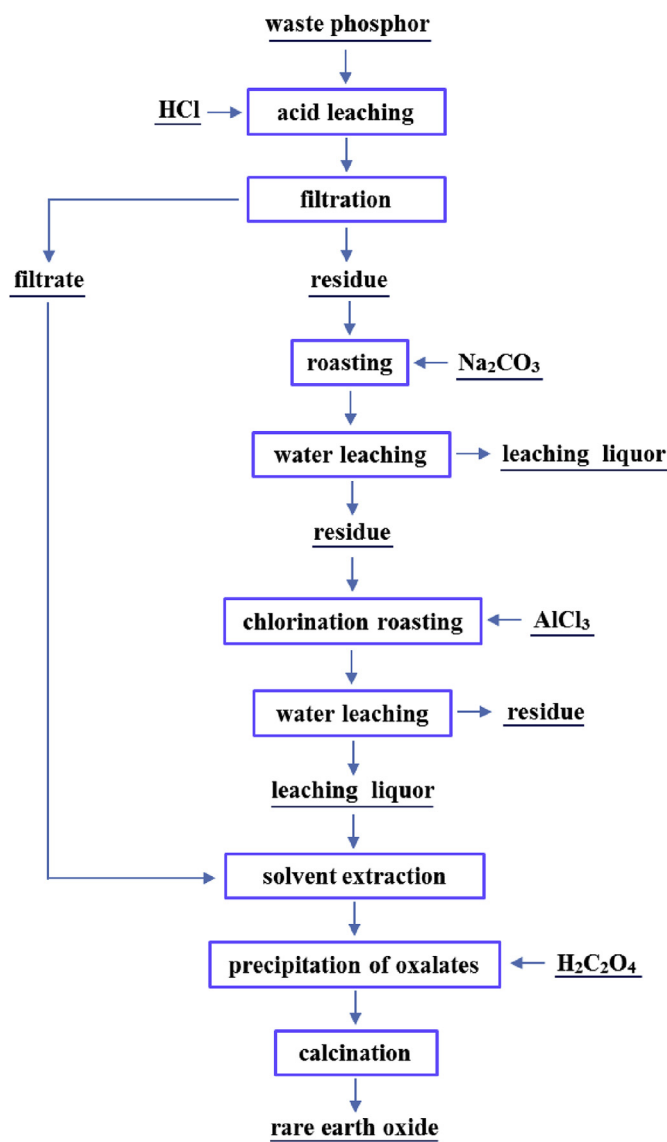
Fig. 11. Illustration of flow-sheet of RE recovery from waste phosphor.

tricolor phosphor, a new complete process route for recycling REEs from the waste phosphor is proposed, as shown in Fig. 11. Considering that Y$_2$O$_3$: Eu^{3+} is acid soluble (Wu et al., 2014), thus the REEs in red phosphor can be firstly extracted out by dissolving in an inorganic acid solution. Then, by decomposition roasting with Na$_2$CO$_3$, the REEs in spinel aluminate can be fully converted to their oxides, and coexist in the roasted product with the unreacted α-Al$_2$O$_3$. However, it is difficult to separate CeO$_2$ from α-Al$_2$O$_3$ because they are hardly attacked in conventional acid leaching (Li et al., 2015; Wang et al., 2015). AlCl$_3$ is a powerful chlorinating agent (Abbasalizadeh et al., 2013), and can chlorinate REE oxides to their chlorides (Zhang et al., 2014). And thus, α-Al$_2$O$_3$, which will not be chlorinated by AlCl$_3$ during chlorination roasting, could be easily removed by leaching in water. Subsequently, the REE chlorides will be separated from each other using the conventional solvent extraction. The REEs in the separated solutions can then be precipitated as oxalates by the addition of oxalic acid. This approach is widely adopted for the production of single REE oxide in industrial practice, because REE oxalates have very limited solubility in a non-oxidizing acid, and more importantly, they are easy to filter and separate from impurities. Finally, the obtained REE oxalates can be decomposed to oxides by direct calcination in air atmosphere. It should be noted that the oxalates may partly convert to carbonates during

calcination. To achieve the complete decomposition of REE oxalates to pure oxides, the oxalates should be calcined at 850–900 °C for 1.5–2 h (Shi, 2015). The proposed recycling route will be further investigated in the future work.

During the whole recycling process, α-Al$_2$O$_3$, an abundant ingredient of aluminate phosphor, is almost unreacted, resulting in less consumption of chemical reagents and less release of effluent and solid residues. Therefore, compared with existing technologies, the proposed recycling route can be regarded as a promising process for waste phosphor recycling in the sense of cost saving and environment protection. Of course, all the process steps in the present recycling route also involve materials and energy consumption, and inevitably have some emissions of gas, water and solid releases. So, prior to its implementation, a comprehensive sustainability assessment should be conducted to achieve the minimization of environmental burdens in the whole recycling route. Life Cycle Assessment (LCA), the most popular and proven method in sustainable product development (Adibi et al., 2014; Vahidi and Zhao, 2017), should be performed by subsequent work to evaluate the potential environmental impacts of the whole recycling operations, and thus help to optimize the proposed recycling route for achieving a better REEs sustainability.

4. Conclusion

In the present work, the thermal decomposition behavior of green phosphor in Na$_2$CO$_3$ assisted roasting was studied by thermodynamic calculations and systematic experiments and sample analyses. The main conclusions could be drawn as follows.

The stable spinel structure of Ce$_{0.67}$Tb$_{0.33}$MgAl$_{11}$O$_{19}$ can be decomposed by roasting with Na$_2$CO$_3$. At 800 °C, the green phosphor begins to react slowly with solid Na$_2$CO$_3$. The reaction is dramatically accelerated when the roasting temperature goes up to the melting point of Na$_2$CO$_3$ (around 857.5 °C in the present experiment), accompanied by a sudden weight loss due to the release of CO$_2$ gas.

Ce$_{0.67}$Tb$_{0.33}$MgAl$_{11}$O$_{19}$ in the green phosphor could be completely decomposed to generate simple oxides of CeO$_2$, Tb$_2$O$_3$ and MgO when roasting with an equivalent mass of Na$_2$CO$_3$ at 1000 °C for 2 h. However, α-Al$_2$O$_3$, an abundant phase existed in the green phosphor, is hardly attacked by Na$_2$CO$_3$ under the roasting conditions. The difference in chemical reactivity allows for Na$_2$CO$_3$ to be effectively used for the decomposition of Ce$_{0.67}$Tb$_{0.33}$MgAl$_{11}$O$_{19}$ only.

Morphological analyses indicated that the decomposition behavior of Ce$_{0.67}$Tb$_{0.33}$MgAl$_{11}$O$_{19}$ in molten Na$_2$CO$_3$ can be elucidated by the unreacted shrinking core model, and the reaction rate constant was estimated to be 4.2×10^{-10} m s^{-1}. The synergistic effect of cation-oxoanion is likely to be responsible for extracting CeO$_2$ and Tb$_2$O$_3$ from the green phosphor via Na$_2$CO$_3$ assisted roasting.

Considering the increasing roles of REEs in high-tech and green technologies, REE recycling from waste not only can mitigate the REE supply risk, but can also minimize the environmental implication in REE production. With the experimental results in the present study, a new and more efficient REE recycling technology for waste phosphor was proposed. Compared with the technologies currently available, the present technology shows better economic and environmental benefits, because α-Al$_2$O$_3$, the main ingredient of waste aluminate phosphor, is almost unreacted throughout the whole recycling process, and thus can be reclaimed through purification. It is worth mentioning that as a new recycling route for REEs, it should not only have a high resource efficiency, but it should also minimize the environmental impacts. In particular, it should avoid the occurrence of secondary environmental pollution and consumption of other critical resources. However, the commercialization of the newly developed recycling route can be better judged after a thorough environmental impacts assessment such as LCA, has been performed to verify the overall environmental benefits.

References

Abbasalizadeh, A., Seetharaman, S., Teng, L., Sridhar, S., Grinder, O., Izumi, Y., Barati, M., 2013. Highlights of the salt extraction process. JOM 65, 1552–1558.

Adibi, N., Lafhaj, Z., Gemechu, E.D., Sonnemann, G., Payet, J., 2014. Introducing a multi-criteria indicator to better evaluate impacts of rare earth materials production and consumption in life cycle assessment. J. Rare Earths 32, 288–292.

Alam, M.A., Zuga, L., Pecht, M.G., 2012. Economics of rare earth elements in ceramic capacitors. Ceram. Int. 38, 6091–6098.

Bi, S., 2006. Alumina Production. Chemical Industry Press, Beijing, pp. 227–228 (in Chinese).

Binnemans, K., Jones, P.T., Blanpain, B., Van Gerven, T., Yang, Y., Walton, A., Buchert, M., 2013. Recycling of rare earths: a critical review. J. Clean. Prod. 51, 1–22.

Burgess, W.A., Keller, M.J., Lekse, J.W., Howard, B.H., Roth, E.A., Granite, E.J., 2018. Effect of pre-reaction ball milling on kinetics of lanthanum phosphate roasting with sodium carbonate. Ind. Eng. Chem. Res. 57, 6088–6096.

Cui, W., Li, P., Wang, Z., Zheng, S., Zhang, Y., 2018. Adsorption study of selenium ions from aqueous solutions using MgO nanosheets synthesized by ultrasonic method. J. Hazard Mater. 341, 268–276.

De Oliveira, W.C.M., Rodrigues, G.D., Mageste, A.B., De Lemos, L.R., 2017. Green selective recovery of lanthanum from Ni-MH battery leachate using aqueous two-phase systems. Chem. Eng. J. 322, 346–352.

De Michelis, I., Ferella, F., Varelli, E.F., Veglio, F., 2011. Treatment of exhaust fluorescent lamps to recover yttrium: experimental and process analyses. Waste Manag. 31, 2559–2568.

Favot, M., Massarutto, A., 2019. Rare-earth elements in the circular economy: the case of yttrium. J. Environ. Manag. 240, 504–510.

Feng, Z., Zhuang, W., Huang, X., Wen, X., Hu, Y., 2010. Effect of MgF_2-H_3BO_3 flux on the properties of (Ce, Tb) $MgAl_{11}O_{19}$ phosphor. J. Rare Earths 28, 351–355.

Hua, Z., Wang, J., Wang, L., Zhao, Z., Li, X., Xiao, Y., Yang, Y., 2014. Selective extraction of rare earth elements from NdFeB scrap by molten chlorides. ACS Sustain. Chem. Eng. 2, 2536–2543.

Janz, G.J., Saegusa, F., 1963. Molten carbonates as electrolytes: viscosity and transport properties. J. Electrochem. Soc. 110, 452–456.

Ji, Y., Shen, S., Liu, J., Xue, Y., 2017. Cleaner and effective process for extracting vanadium from vanadium slag by using an innovative three-phase roasting reaction. J. Clean. Prod. 149, 1068–1078.

Kumari, A., Panda, R., Jha, M.K., Lee, J.Y., Kumar, J.R., Kumar, V., 2015. Thermal treatment for the separation of phosphate and recovery of rare earth metals (REMs) from Korean monazite. J. Ind. Eng. Chem. 21, 696–703.

Leblebici, M.E., Kuhn, S., Stefanidis, G.D., Van Gerven, T., 2016. Milli-channel mixer and phase separator for solvent extraction of rare earth elements. Chem. Eng. J. 293, 273–280.

Li, R.Q., Wu, Y.F., Zhang, Q.J., Wang, W., 2012. Extraction of rare earth from waste three primary colors fluorescent powder in high temperature alkali fusion method. In: Proceedings of CCATM' 2012 International Conference & Exhibition on Analysis & Testing of Metallurgical Process & Materials, vol. 32. pp. 795–799.

Li, X., Liu, X., Qiao, X., Xing, S., 2015. Confining the polymerization of aniline to generate yolk–shell polyaniline@SiO$_2$ nanostructures. RSC Adv. 5, 79172–79177.

Liang, Y., 2003. Carbon Dioxide Capture from Flue Gas Using Regenerable Sodium-Based Sorbents. Louisiana State University, Baton Rouge, LA.

Liang, Y., Harrison, D.P., Gupta, R.P., Green, D.A., McMichael, W.J., 2004. Carbon dioxide capture using dry sodium-based sorbents. Energy Fuels 18, 569–575.

Liang, Y., Liu, Y., Lin, R., Liao, C., 2016. Leaching of rare earth elements from waste lamp phosphor mixtures by reduced alkali fusion followed by acid leaching. Hydrometallurgy 163, 99–103.

Liu, H., Zhang, S., Pan, D., Liu, Y., Liu, B., Tian, J., 2015. Mechanism of

CeMgAl$_{11}$O$_{19}$:Tb^{3+} alkaline fusion with sodium hydroxide. Rare Met. 34, 189–194.

Liu, Y.F., Zhang, S.G., Liu, B., Shen, H.L., 2017. An alkaline fusion mechanism for aluminate rare earth phosphor: cation–oxoanion synergies theory. Rare Met. 1, 1–7.

Lu, N., Likos, W.J., 2004. Unsaturated Soil Mechanics. John Wiley & Sons Inc, New York, pp. 328.

Luo, H., Kanoh, H., 2017. Fundamentals in CO$_2$ capture of Na$_2$CO$_3$ under a moist condition. J. Energy Chem. 26, 972–983.

Mei, G., Rao, P., Matsuda, M., Fujita, T., 2009. Separation of red (Y$_2$O$_3$:Eu^{3+}), blue (BaMgAl$_{10}$O$_{17}$: Eu^{2+}) and green (CeMgAl$_{10}$O$_{17}$:Tb^{3+}) rare earth phosphors by liquid/liquid extraction. J. Wuhan Univ. Technol. 24, 603–607.

Moldoveanu, G.A., Papangelakis, V.G., 2012. Recovery of rare earth elements adsorbed on clay minerals: I. Desorption mechanism. Hydrometallurgy 117–118, 71–78.

Pemba-Mabiala, J.M., Lenzi, M., Lenzi, J., Lebugle, A., 1990. XPS study of mixed cerium–terbium orthophosphate catalysts. Surf. Interface Anal. 15, 663–667.

Rabah, M.A., 2008. Recyclables recovery of europium and yttrium metals and some salts from spent fluorescent lamps. Waste Manag. 28, 318–325.

Rajak, D.K., Guria, C., Ghosh, R., Agarwal, S., Pathak, A.K., 2016. Alkali assisted dissolution of fly ash: a shrinking core model under finite solution volume condition. Int. J. Miner. Process. 155, 106–117.

Sarkar, B., Singha, R.K., Tiwari, R., Ghosh, S., Acharyya, S.S., Pendem, C., Konathala, L.N.S., Bal, R., 2014. Preparation of CeO$_2$ nanoparticles supported on 1-D silica nanostructures for room temperature selective oxidation of styrene. RSC Adv. 4, 5453–5456.

Shi, F., 2015. Rare Earth Metallurgy Technology, second ed. Press of Metallurgy Industry, Beijing (in Chinese).

Slavinskaya, E.M., Veniaminov, S.A., Notté, P., SIvanova, A., Boronin, A.I., Chesalov, Y.A., A Polukhina, I., Noskov, A.S., 2004. Studies of the mechanism of ammonia oxidation into nitrous oxide over MnBiO/α-Al$_2$O$_3$ catalyst. J. Catal. 222, 129–142.

Sun, C., Li, H., Wang, Z., Chen, L., Huang, X., 2004. Synthesis and characterization of polycrystalline CeO$_2$ nanowires. Chem. Lett. 33, 662–663.

Takahashi, T., Takano, A., Saitoh, T., Nagano, N., Hirai, S., 2011. Separation and recovery of rare earth elements from phosphor sludge in processing plant of waste phosphor lamp by pneumatic classification and sulfuric acidic leaching. J. Min. Mater. Proc. Inst. Jpn. 177, 579–585.

Tan, Q., Li, J., Zeng, X., 2015. Rare earth elements recovery from waste fluorescent lamps: a review. Crit. Rev. Environ. Sci. Technol. 45, 749–776.

Tang, Y., Zhu, X., Wang, H., Qi, F., 2006. Progress in research on barium magnesium aluminate. Mater. Rev. 20, 335–338 (in Chinese).

Vahidi, E., Zhao, F., 2017. Environmental life cycle assessment on the separation of rare earth oxides through solvent extraction. J. Environ. Manag. 203, 255–263.

Wang, L., Guo, Z., Chi, J., Wang, Y., Chen, D., 2015. Progress in multipurpose research and development of multiform alumina. Iorg. Chem. Ind. 47, 11–16 (in Chinese).

Wu, J., Wang, J., Du, Y., Li, H., Jia, X., 2016. Adsorption mechanism and kinetics of azo dye chemicals on oxide nanotubes: a case study using porous CeO$_2$ nanotubes. J. Nanoparticle Res. 18, 191.

Wu, Y., Yin, X., Zhang, Q., Wang, W., Mu, X., 2014. The recycling of rare earths from waste tricolor phosphors in fluorescent lamps: a review of processes and technologies. Resour. Conserv. Recycl. 88, 21–31.

Xiu, Z., Xing, Z., Li, Z., Wu, X., Yan, X., Hu, M., Cao, Y., Yang, S., Zhou, W., 2018. Ti^{3+}-TiO$_2$/Ce^{3+}-CeO$_2$ nanosheet heterojunctions as efficient visible-light-driven photocatalysts. Mater. Res. Bull. 100, 191–197.

Yang, Y.M., Deng, S.H., Xie, F.H., Lan, Q.F., Shen, W.M., Huang, Z.H., 2012. Technical study on rare earth recovery from fluorescent powder scrap. Nonferrous Met. 10, 23–26 (In Chinese).

Yu, W., Tang, Q.Y., Chen, J.A., Sun, T.C., 2016. Thermodynamic analysis of the carbothermic reduction of a high-phosphorus oolitic iron ore by FactSage. Int. J. Min. Met. Mater. 23, 1126–1132.

Zhang, M., Wang, H., Han, W., Zhang, M., Li, Y., Wang, Y., Xue, Y., Ma, F., Zhang, X., 2014. Electrochemical extraction of cerium and formation of Al-Ce alloy from CeO$_2$ assisted by AlCl$_3$ in LiCl-KCl melts. Sci. China Chem. 57, 1477–1482.

Zhang, Q., Lu, J., Saito, F., 2000. Selection extraction of Y and Eu by non-thermal acid leaching of fluorescent powder activated by mechanochemical treatment using a planetary mill. J. Min. Mater. Proc. Inst. Jpn. 116, 137–140.

Zhang, S., Li, Y., Lv, Y., Fan, L., Hu, Y., He, M., 2017. A full-color emitting phosphor Ca$_9$Ce(PO$_4$)$_7$:Mn^{2+},Tb^{3+}: efficient energy transfer, stable thermal stability and high quantum efficiency. Chem. Eng. J. 322, 314–327.

Zhang, S., Liu, H., Pan, D., Tian, J., Liu, Y., Volinsky, A.A., 2015. Complete recovery of Eu from BaMgAl$_{10}$O$_{17}$:Eu^{2+} by alkaline fusion and its mechanism. RSC Adv. 5, 1113–1119.

Zhang, Z., Wang, R., Xiong, J., Wen, G., Liao, G., Xie, B., 2016. Effect of alkaline fusion pretreatment on extraction rate of rare earth from waste rare earth fluorescent powder. Nonferr. Met. Sci. Eng. 7, 129–135 (in Chinese).